Science
AAAS

Supplementary Materials for

Predictive grid coding in the medial entorhinal cortex

Ayako Ouchi and Shigeyoshi Fujisawa

Corresponding author: Shigeyoshi Fujisawa, shigeyoshi.fujisawa@riken.jp

Science **385**, 776 (2024)
DOI: 10.1126/science.ado4166

The PDF file includes:

Materials and Methods
Figs. S1 to S10
Table S1
References

Other Supplementary Material for this manuscript includes the following:

MDAR Reproducibility Checklist

Materials and Methods

Behavioral procedures

All experimental protocols were approved by the Institutional Animal Care and Use Committee of RIKEN. Six-week-old male Long-Evans rats were purchased from Japan SLC, Inc. (Shizuoka, Japan). The rats were housed in a temperature-controlled room (20-22℃) under a light-dark cycle (lights on from 8:00 to 20:00). After 5-7 days of environmental habituation, the rats were subjected to a water deprivation schedule and started training on the behavioral task (7-8 weeks old at the start of training).

Goal-directed behavioral task

Six rats were trained in a goal-directed behavioral task (Fig. 1A; Fig. S1) for electrophysiological recording (rat IDs: o28, o30, o31, o32, o34, and o36). The behavioral experiments were conducted in an open field of 210×210 cm that was surrounded by 40cm height fences. Visual cues were placed in the center of each fence in each direction. Two movable water ports (D2 × H1.5 cm) were set in the open field, which was connected to micropumps (Type 7615; Christian Bürkert GmbH & Co. KG, Ingelfingen, Germany) that delivered 0.2% saccharin water (M5N1991; Nacalai Tesque, Kyoto, Japan) as a reward. The rats were rewarded with water drops (25 μl) for alternating visits to the two ports. The infrared sensors (LR-TB5000CL; Keyence, Osaka, Japan) were placed above the water ports to detect the time of arrival and departure of the rats. Each block consisted of 20-30 trials of round trips between two ports. The locations of the water ports varied for each block, as indicated in Fig. 1A. The possible locations of the pairs of the water ports were shown in Fig. S1C. There were also additional blocks in which the two ports were placed diagonally. A single session of this task lasted approximately 1 hour. The behavioral experiments were automatically controlled by the custom-written LabVIEW (National Instruments, Austin, TX) programs running on a Windows personal computer located outside of the field. The rats were trained on this task for 2-3 weeks before surgery.

A series of goal-directed and random foraging tasks

Three rats were trained in a series of goal-directed (short version) and random foraging tasks for electrophysiological recording (Fig. 4) (rat IDs: o44, o45, and o46). In each session, the rats performed the goal-directed task (short version) and then sequentially performed a random foraging task in the same open field environment. The apparatus and procedure for the goal-directed task (short version) were the same as described above, but each block consisted of 10-15 trials, which was approximately half of the full-length goal-directed behavioral task. In the random foraging task, the water ports used in the goal-directed task were removed from the open field. The rats freely explored randomly placed chocolate cereals that were moistened with water in the open field for approximately 40 min. The maximum capacity of the chocolate cereal was roughly 2 g per session. Because of the different task configurations, we analyzed separately the data from the six rats that performed the full-length goal-directed behavior and the data from the three rats that performed a series of goal-directed (short version) and random foraging tasks (Table S1). The data from the three rats were used in Fig. 4 and Fig. S6.

Surgery and recording

Nine rats were surgically implanted with silicon probes (rat-IDs: o28, o30, o31, o32, o34, o36, o44, o45, and o46) for the chronic recording of neuronal activity during the tasks. General surgical procedures for chronic recordings have been described previously (*19, 20*). In this study, we used P128-8 silicon probes (Diagnostic Biochips Inc., Glen Burnie, MD) consisting of 8 shanks (150-µm shank spacing). Each shank had 16 recording sites (~1 MΩ impedance), staggered to provide a two-dimensional arrangement (30 µm vertical separation; Fig. S6B). The rats were implanted with two silicon probes in the entorhinal cortex (the target coordinate was anterior-posterior (AP) = -8.67 mm, medial-lateral (ML) = 4.3 mm, and dorsal-ventral (DV) = 2.65 mm), and the CA1 region of the hippocampus (AP = -3.6 mm, ML = 2.8 mm, and DV =1.4 mm) in the same hemisphere. The shanks were oriented parallel to the anterior-posterior axis for the entorhinal cortex and were aligned parallel to the septotemporal axis for the hippocampus (i.e., 45 degrees parasagittal), respectively. The silicon probes were placed approximately 0.5 mm above the target coordinates at the time of surgery and gradually inserted daily to the desired depth positions using the attached micromanipulator.

During the recording sessions, the wide-band neurophysiological signals were recorded continuously at 20 kHz on the Intan RHD 1024-channel recording controller (Intan Technologies, Los Angeles, CA). For LFP analysis, signals downsampled to 1.25 kHz were used. Spike sorting was performed semi-automatically with Kilosort2, followed by manually adjusting the clusters with Phy2 (*56*). The tips of the probes were moved spontaneously or manually by the experimenter between sessions. However, we could not exclude the possibility that some neurons that were recorded in different sessions were identical because spikes from sessions recorded on different days were clustered separately. Thus, the total number of independent neurons may have been overestimated.

Rat behavior was monitored using a USB camera with a CMOS sensor (acA720-520; Basler AG, Ahrensburg, Germany) set on the ceiling. The capturing times of video frames were simultaneously recorded with electrophysiological data to synchronize the physiological and behavioral data in the post hoc analyses. The positional information of the rat's head was subtracted from the video frames using the DeepLabCut software (*57*).

After all the recording sessions were completed, a small current (5-7.5 µA for 10 to 12 s) was passed through the recording electrodes of the probe two days prior to sacrificing the animals to identify the recording sites. The rats were deeply anesthetized and perfused through the heart with PBS, followed by a 4% paraformaldehyde solution. The brains were sectioned by a slicer (PRO10; Dosaka EM, Kyoto, Japan) at 100 µm in the sagittal plane. Sections were stained with fluorescent Nissl, mounted on slides, and cover-slipped. The images were captured with a research slide scanner (Slideview VS200; Evident, Tokyo, Japan) with ×10 resolution. The traces of the silicon probe shanks were reconstructed from multiple sections (Fig. 1C, Fig. S6F).

Data analysis

All analyses after spike sorting were performed with custom-written programs in MATLAB (MathWorks, Natick, MA). We used the Circular Statistics Toolbox (*58*) for circular analyses and statistics.

Firing rate maps and spatial autocorrelation

A two-dimensional firing rate map of each unit was constructed by calculating the spikes divided by occupancy time for each 3cm x 3cm bin of position data, followed by applying smoothing with a two-dimensional convolution with a Gaussian kernel. The spatial autocorrelation of a rate map was calculated using Pearson's product moment correlation coefficient with correction for edge effect and unvisited positions based on the previous studies (*5, 6*). A trial period was defined as the time from departure to arrival detected by the infrared sensors located above the reward ports.

We also constructed rate maps using the position data that were projected to future or past positions (Fig. 1E). To obtain the future or past positions, each position point was projected onto the actual rat trajectory to shift the distance *d* (Fig. 1D). If projection on the trajectory was not possible (e.g., around the goal position of trials), these position points were omitted.

We also constructed rate maps using only selected directions of travel (Fig. 2B). In this analysis, task trials were grouped by direction of travel (i.e., north to south, south to north, east to west, and west to east), and the firing rate map was computed using only the position data for each group of trials.

Analysis of firing rate in linearized positions

A plot of firing rate in the linearized positions was also constructed by direction for each block (Fig. 2B, second right; Fig. S3A). The two-dimensional position data were linearized by projecting a straight line between the start and goal positions. Similar to a two-dimensional firing rate map, a one-dimensional firing rate plot was made by calculating the spikes divided by the occupancy time for each 0.01 bin of normalized position, followed by applying smoothing with a convolution with a Gaussian kernel. Here, normalized position 1 corresponds to the length of one side of the open field (i.e., 210 cm).

We also made a one-dimensional rate plot aligned by the peaks of the grid fields (Fig. 2B, right; Fig. S3A). First, we detected local peaks in the rate plot of each block and in each direction. Then, we aligned each peak so that its position became the zero point and averaged the total detected peaks.

Gridness score

To assess the grid structure of the firing rate maps, we calculated gridness scores. First, we calculated the spatial autocorrelation for the smoothed two-dimensional rate map (*5, 6*). Then, we detected the six peaks closest to the center, within 1.5 times the distance to the closest peak in the autocorrelation map. If there were fewer than six peaks, only the detected peaks were used. To modify the elliptical distortion of these six peaks, we applied the algorithms developed by Brandon et al. 2011 (*59*) (referred to as 'gridness measure 3' in their paper). We then extracted ring parts surrounded by two circles; the inner radius was defined as 30 cm from the center of the map, and the outer radius was varied from 33 cm to 120 cm in steps of 1 bin (3 cm). We calculated the Pearson's correlation of each ring part with its rotation in degrees obtained for angles of 60° and 120° on one side and 30°, 90°, and 150° on the other. For each sample, the score was calculated as the minimum difference between any of the elements in the first group and any of the elements in the second group. The gridness score was defined as the best score from these consecutive samples of ring parts (*59, 60*).

To compute the plot of the gridness score as a function of position shift, we calculated the position of the projected location at shift distance *d* ($-55 < d < 55$ cm, step is 0.55 cm) using the

method described above, and the gridness score was calculated at each *d*. The optimal position shift was defined as the location of the peak sought within half the grid spacing in the plus and minus directions, respectively, for each cell.

To estimate the statistical significance of the gridness score, we used the shuffling method. To obtain the surrogate dataset, the position data of the trials were shuffled to the data of other trials, and a surrogate gridness score was computed using the trial-shuffled position data. We repeated this 100 times. If the original gridness score was above 95% of the surrogate dataset, we considered the gridness score to be significant ($P<0.05$).

Analysis of grid spacing and grid orientation

To quantify the grid spacing, we calculated the mean of the distances from the center to the six peaks in the autocorrelation of the firing rate map (Fig. 3E). To estimate the orientation with respect to the arena boundaries for grid cells (*14*), we calculated the direction of the six peaks closest to the center in the autocorrelation of the firing rate map (Fig. 3L). For predictive grid cells, we used the autocorrelation map of the firing rate map at the optimally shifted position for these analyses.

Analysis of LFP

To extract theta phase, LFPs in the CA1 pyramidal cell layers, which were identified by the amplitudes and the polarities of sharp wave ripples (*61*), were filtered with a Butterworth filter with a pass-band range of 4-10 Hz. Instantaneous theta phases were estimated by Hilbert transform of the filtered signals.

The presence of theta phase precession in each neuron was assessed as follows (Fig. S3B): First, we made a rate plot and theta phase plot aligned by the peaks of the grid fields, as described above. The standard deviation σ was calculated over the distribution centered on the peak of the rate plot. The positions were divided into bins from -σ to +σ with a step of σ/5, and the spiking theta phases in each bin were averaged. If the average phase was shifted more than 60 degrees from -σ to +σ, we considered the presence of phase precession.

Criteria for predictive, phase-precessions, and phase-locked grid cells

In this study, we considered regular spiking neurons as those with an average firing rate between 0.8 Hz and 7 Hz during the session and with spatial information (*62*) higher than 0.8 bit/spike (n=3843 units from 6 rats). Spatial information was calculated from a firing rate map for each direction and averaged. We used them in the subsequent analysis

(A) Predictive grid cell criteria were defined as meeting the following conditions: (i) The gridness score at the original location is not significant ($P \geq 0.05$) compared to the shuffled data. (ii) When the gridness score is plotted as a function of location shift, there is a peak location at a future location, and the gridness score at the peak location is significant ($P < 0.05$). (iii) There is no phase precession, and theta phase preference is 180° ± 60° with a peak-to-baseline ratio greater than 20.

(B) Phase-precession grid cell criteria were defined as (i) the gridness score at the original location is significant ($P < 0.05$) compared to the shuffled data, and (ii) phase precession is present (Fig S3B).

(C) Phase-locked grid cell criteria were defined as (i) the gridness score at the original location is significant ($P < 0.05$) compared to the shuffled data, and (ii) there is no phase precession, and theta phase preference is 300° ± 60°.

Analysis of speed tuning

To assess the speed tuning of each cell, we calculated speed scores defined as the Pearson product-moment correlation between the instantaneous firing rate and running speed in 25.6ms time bins, as proposed in the previous report (*8*). For the statistical evaluation of the speed tuning, we used the shuffling procedure while preserving the positional information. As shown in Fig. 3I, there was the relationship between speed and rat position. To rule out the effect of position, we segmented the location into 6cm × 6cm meshes (Fig. 3I) and shuffled the relationship between speed and time labels within each mesh in each block. We repeated this 100 times for each cell. If a neuron's speed correlation from the original data was greater than the 99th percentile of the distribution of all shuffled data, we considered the firing rate of the neuron to be significantly correlated with speed (Fig. 3J).

Analysis of optimal grid shift in each direction

To estimate the optimal grid shift in each direction, we calculated the cross-correlation of the unidirectional map and optimally shifted map including all directions, and then quantified the offset of the cross-correlation peak from the center point (Fig. S5). The search for the peak position in the cross-correlation map was searched within half the grid spacing to the approaching direction of travel. The predictive grid cells that had the peaks in the cross-correlation maps from all four unidirectional maps were used in the analysis (n = 184 cells).

Comparison of position projection methods

We tested the methods of spatial shift for estimating the gridness for the future position. (i) Projection on the rat trajectory with distance *d*, the method we mainly used in this study (Fig 1D). (ii) Accumulation along the trajectory. (iii) Projection on the tangential line of the rat trajectory. (iv) Projection on the line extended in the head direction (Fig. S7). To describe this in more detail, method (i) projected to a point on the trajectory at a linear distance of *d* from the rat's current position; method (ii) projected to a point on the trajectory at a cumulative distance of *d* on the trajectory; in method (iii), the tangent to the trajectory at the rat's current position was calculated and projected to a position point *d* away tangentially away from the current position; in method (iv), the head direction vector at the rat's current position was calculated and projected to a point d away from the current position in the head direction. Note that methods (i) and (ii) projected positions on the rat's actual trajectory, but the projected points in methods (iii) and (iv) are not necessarily on the actual trajectory.

Comparison of time and position shift for future projection

We examined which of the positional or temporal shift was optimal for predicting future spatial information in the predictive grid cells (Fig. S8). To compute the plot of the gridness score as a function of temporal shift, we calculated the position of the projected location at shift time t with a step of 25.6 ms, and the gridness score was calculated at each t. We computed the gridness score as a function of both positional and temporal shift and compared the maximum gridness scores between them (Fig. S8C). In this analysis, we included the predictive grid cells that had a significant gridness score at the peak of both positional and temporal shifts (n = 168 cells).

In addition, we investigated the effect of grid spacing on the relationship between spatial and temporal shifts in the predictive grid cell. To examine the effect of the size of the grid

spacing on the spatial and temporal shift, we sorted the predictive grid cells by their grid spacing and divided them into two groups with large and small grid spacing. The optimal positional and temporal shifts were then compared between the two groups (Fig. S8D-E).

We also examined the effect of speed on the relationship between spatial and temporal shifts in the predictive grid cell. To examine the effect of running speed on spatial and temporal shift, firing spikes were sorted by the speed in each predictive grid cell while preserving the positional information. As shown in Fig. S8F, there was a relationship between speed and rat position. To rule out the influence of the correlation between position and speed, we segmented the location into 6cm × 6cm meshes (Fig. S8F). We sorted the spikes by the speed at which the spike occurred within each mesh in each block and divided them into two groups with high and low speeds. The optimal positional and temporal shifts were then compared between the two groups (Fig. S8F-G).

Layer identification of the MEC neurons

We performed analyses to determine in which layers of the MEC the recorded units were located (Fig. S6). First, to anatomically identify where the shanks were placed in the MEC, a current lesion was made on the last day of recording in each animal, followed by Nissl staining of the brain sections (Fig. S6A), as described above. In addition, electrophysiological analysis was also performed in each session for the purpose of more precise location determination. Figure S6C shows the CSD of the averaged theta oscillation calculated in the direction orthogonal to the layer. As reported in the previous studies, phase reversal was observed between layer 1 and layer 2 (*63, 64*). Figure S6D shows a two-dimensional CSD based on all channels of all shanks in the MEC, which shows that both anatomical and electrophysiological features are well matched. Using the anatomical and electrophysiological analysis, we identified the location of each cell in the layer of the MEC based on the electrode position where the maximum potential of the cell was obtained (Fig. S6E).

Overall firing rate distribution

To calculate the overall firing rate distribution (Fig. 3N), the rate plot in the linearized positions was first calculated in each direction of each block and then averaged and normalized for each neuron. Overall averages were then calculated for all predictive, phase-precession, and phase-locked grid cells, respectively.

Permutation tests

Permutation tests were used to identify conditional differences in firing rates or decoded positions (Figs. 3N & 5F). Detailed information on this method is provided in the previous publications (*58*). Briefly, the mean rate plot from the start to goal positions in the normalized position was estimated in each neuron in each type of grid cell (Fig 3J; e.g., the mean firing rates of predictive and phase-precession grid cells; $\lambda_{\mathrm{pred}}(t)$ and $\lambda_{\mathrm{phaseprec}}(t)$). Then, the difference of the rates, $D_0(t) = \lambda_{\mathrm{pred}}(t) - \lambda_{\mathrm{phaseprec}}(t)$, was computed. The labels of the neuron types were randomly permuted, and the mean rate plots and the statistic $D_1(t)$ under the permuted labels were re-estimated. This process was repeated *R* times to obtain the statistic from the original data, $D_0(x)$, along with the statistic from the resampled data, $D_1(t)$, …, $D_R(t)$. Using this resampled (shuffled) data set, a pointwise p-value (5% for both sides, i.e., 2.5% for upper and lower) was computed at each point. To avoid multiple comparison issues, we also computed the

global 5% bands (*58*). The permutation tests were also used to assess the significance of the differences in decoded position between the data including and excluding the predictive grid cells (Fig. 5F).

Data analysis for a series of goal-directed and random foraging tasks

Three rats performed a series of goal-directed (short version) and random foraging tasks in the same environment on the same days, as described above. We applied spike sorting to the data containing both tasks on each day, allowing us to observe the activity of the same units in the both tasks. The procedure of the analysis was the same as the analysis of the data obtained in the full-length goad-directed behavior task. For the group analysis in Fig. 4D-F, we used the neurons that met the criteria of predictive, phase-precession, and phase-locked grid cells in the goal-directed task (short version) (n = 143, 44, and 48 cells from 3 rats, respectively). For the group analysis in Fig. 4G-I, in addition to the above criteria for Fig. 4D-F, we used the neurons that had a significant grid score at the peak of the optimal shift in the random foraging task data to compare the grid properties between the goal-directed and random foraging tasks (n = 53, 42, and 48 cells, respectively).

Reconstruction of rat's position from neuronal activities

A memoryless Bayesian decoding algorithm was used to estimate the rat's positions in the task trials (Fig. 5; *17-20, 65*). In this analysis, we used firing rate maps of neurons as a prior template and spiking activity of neurons in 10 ms bins as to compute a posterior. Here, neuronal activity of predictive, phase-precession, and phase-locked grid cells was used. The firing rate maps at the optimally shifted position with were used as prior templates for predictive, phase-precession, and phase-locked grid cells. Based on Bayes' theory, the posterior probability of the two-dimensional position ($\boldsymbol{x}$) given spike trains from single neurons (spikes) was estimated as:

$$P(\boldsymbol{x}|spikes) = \frac{P(spikes|\boldsymbol{x}) \cdot P(\boldsymbol{x})}{P(spikes)}$$

The likelihood was estimated under the assumption of Poisson firing statistics and independent rates, as:

$$\begin{aligned} P(spikes|\boldsymbol{x}) &= \prod_{i=1}^{N} P(n_i|\boldsymbol{x}) \\ &= \prod_{i=1}^{N} \frac{(\tau f_i(\boldsymbol{x}))^{n_i}}{n_i!} exp(-\tau f_i(\boldsymbol{x})) \end{aligned}$$

where τ is the time window of sampling spike trains (10ms was used in this study), $f_i(\boldsymbol{x})$ is the firing rate maps at the highest gridness scores of the i-th unit, n_i is the number of spikes of the i-th unit in the time window, and N is the total number of units. Combining these equations, the posterior probability of the position was computed as:

$$P(\boldsymbol{x}|spikes) = C \cdot P(\boldsymbol{x}) \left(\prod_{i=1}^{N} \frac{(\tau f_i(\boldsymbol{x}))^{n_i}}{n_i!} \right) exp\left(-\tau \sum_{i=1}^{N} f_i(\boldsymbol{x}) \right)$$

where C is a normalization factor that depends on τ and the number of spikes of each neuron (*65*). To construct theta sequences, the decoded probabilities across trials were aligned with the theta phases calculated from simultaneously recorded LFP (CA1 theta) and were averaged (*17-19*).

In Fig. 5D, the probability density of the decoded position at each time bin was aligned with the original position and head direction at which the spikes were sampled. In Fig. 4F, the most probable position was taken as the decoded position, i.e., $\hat{\boldsymbol{x}} = \text{argmax } P(\boldsymbol{x}|spikes)$, to account for session-to-session variability. For the group analyses, we selected the sessions in which more than 4 predictive grid cells and more than 4 other types of grid cells were simultaneously recorded (n=25 sessions from 4 rats; Table S1).

Theta cycle swapping method

With regard to the theta sequence revealed in the analysis of Fig 5, we investigated whether the theta sequence was organized as a result of synchronized activity of cells within the theta cycle or as a result of independent activity of each cell (Fig. S9). To address this, we used a theta cycle swapping method. In this method, each spike of each cell is moved randomly to a theta cycle of $\pm k$ cycle apart (k=1 or 2), preserving theta phase at the spike time (Fig. S9B). We applied this theta cycle swapping method to the spikes of all three types of grid cells, and then we computed the theta sequence with the method described above using the surrogate datasets and compared it to the original data (Fig. S9; see also Fig. 5F; n=25 sessions from 4 rats; Table S1).

Pairwise analysis of predictive grid cells and CA1 place cells

To study the functional connectivity between predictive grid cells and CA1 place cells, we analyzed the relationship between information representation and spike timing between these cells. Specifically, we analyzed the difference in the positions of the spatial receptive fields in each cell pair and the difference in spike timing calculated from the CCG (Fig. S6A). Because grid cells and place cells often have multiple peaks in their place fields (or grid fields), calculations were performed for each peak of each cell of the cell pair (Fig. S6B). The computational procedure was as follows: (1) For each cell, we made a one-dimensional firing rate plot in the linearized position for each direction of each block and detected the peaks. (2) Focusing on one peak for each cell, we calculate CCGs using the spikes contained in each peak of the cell pair. If the number of spike pairs within ±50ms was more than 50 counts, the pair of the peaks was used for the successive analysis. (3) We tested whether the CCG peak of each peak of the pair had significantly high (i.e., significant functional connectivity) compared to the surrogate dataset. To this end, we used the spike jittering method (*66*). Briefly, spikes of one of the neurons were time jittered by -50 to 50 msec to generate a jittered cross-correlogram (jittered). By repeating the procedure 1000 times, the 99% confidence intervals for each bin (P = 0.01) are calculated. If the CCG peak value exceeded the line, we considered it as significant (P < 0.01). The same analysis was also applied to the pairs of predictive and phase-precession grid cells and the pairs of predictive and phase-locked grid cells.

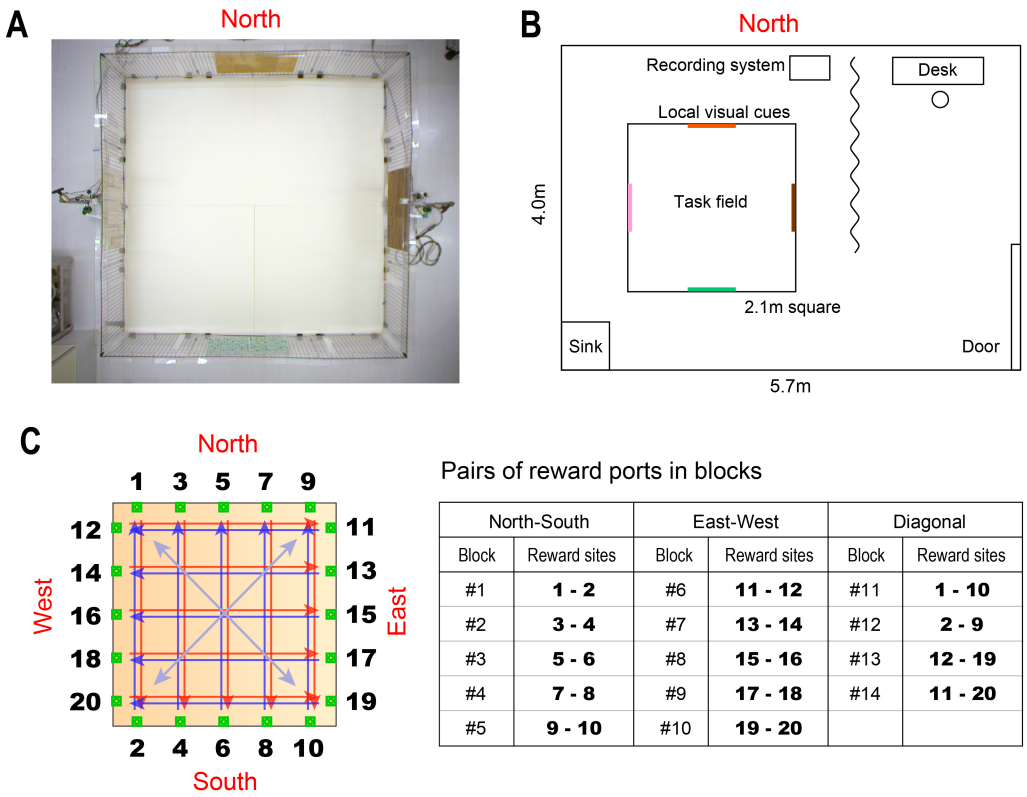

Pairs of reward ports in blocks

North-South		East-West		Diagonal	
Block	Reward sites	Block	Reward sites	Block	Reward sites
#1	**1 - 2**	#6	**11 - 12**	#11	**1 - 10**
#2	**3 - 4**	#7	**13 - 14**	#12	**2 - 9**
#3	**5 - 6**	#8	**15 - 16**	#13	**12 - 19**
#4	**7 - 8**	#9	**17 - 18**	#14	**11 - 20**
#5	**9 - 10**	#10	**19 - 20**		

Fig. S1. Detailed schematic of the goal-directed behavioral task.

(A) A photograph of the open field used in the task. The behavioral experiments were conducted in an open field of 210×210 cm that was surrounded by 40cm height fences. Visual cues were placed in the center of each fence in each direction.
(B) Schematic of the experimental room.
(C) Positions of possible reward locations. (Right) The table of all possible pairs of reward ports in the task blocks.

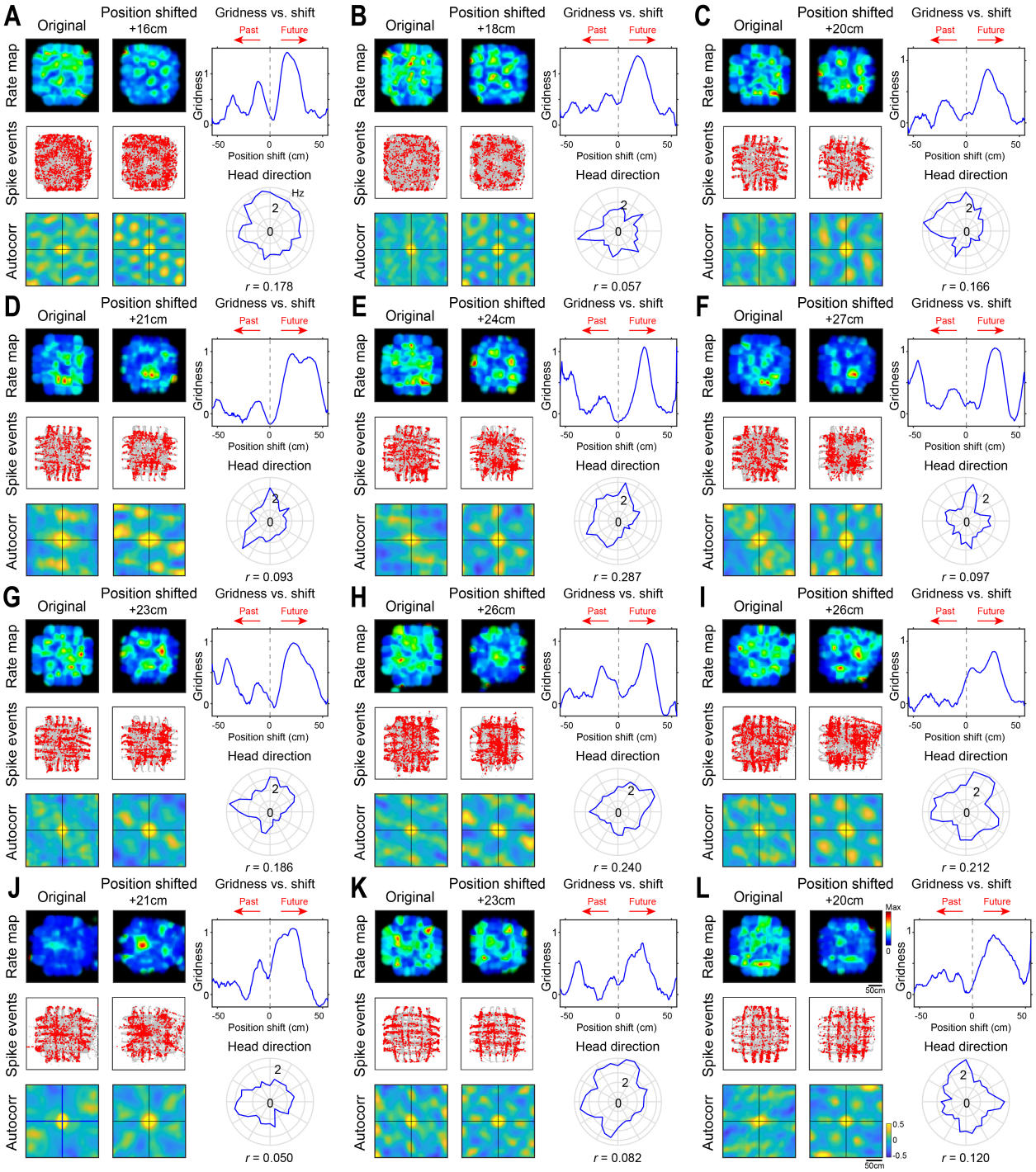

Fig. S2. Grid representation for future spatial information in the entorhinal cortex.

Twelve examples of predictive grid cells (see also, Fig 1E). (Left) Firing rate maps (top), spiking events (red) on rat's trajectories (gray) (middle), and their spatial autocorrelation (bottom), whose positional references were original and future projected. (Right top) Gridness scores as a function of reference positions. A positive position shift indicates a future position and a negative indicates a past position. (Right bottom) Firing rate modulation is by the head direction. The mean resultant length was indicated as *r*.

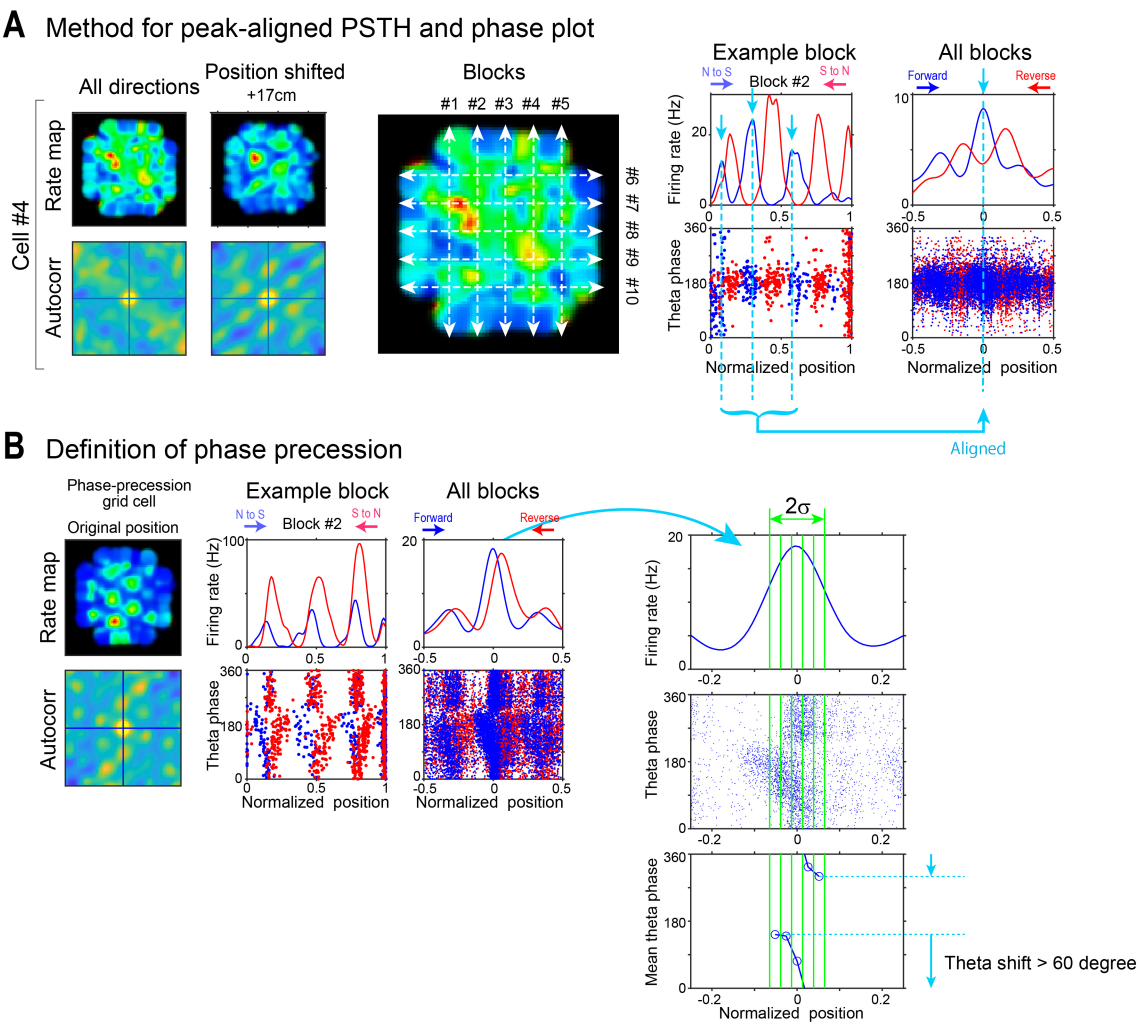

Fig. S3. Methods for analyzing firing rates and theta phases in the linearized positions.

(A) Method for plotting firing rates and theta phases in the linearized positions. First, the two-dimensional positional data were linearized by projecting a straight line between the start and goal positions. The firing rate in the linearized positions was calculated by each direction for each block. Similar to two-dimensional firing rate maps, a rate plot in the linearized position was created by calculating the spike numbers divided by the occupancy time for each 0.01 bin of normalized position, followed by applying smoothing with a convolution with a Gaussian kernel. In a plot of the linearized positions, normalized position 1 corresponds to the length of one side of the open field (i.e., 210 cm). We also created a one-dimensional rate plot aligned by the peaks of the grid fields (right). First, we detected local peaks in the rate plot of each block and in each direction. Then, we aligned each peak so that its position became the zero point and averaged the overall detected peaks.

(B) The presence of theta phase precession in each neuron was assessed as follows: First, we made a rate plot and theta phase plot aligned by the peaks of grid fields, as described above. The standard deviation σ was calculated over the distribution centered on the peak of the rate plot. The positions were divided into bins from -σ to +σ with a step of σ/5, and the spiking theta phases were averaged in each bin. If the average phase was shifted more than 60 degrees from -σ to +σ, we considered the presence of phase precession.

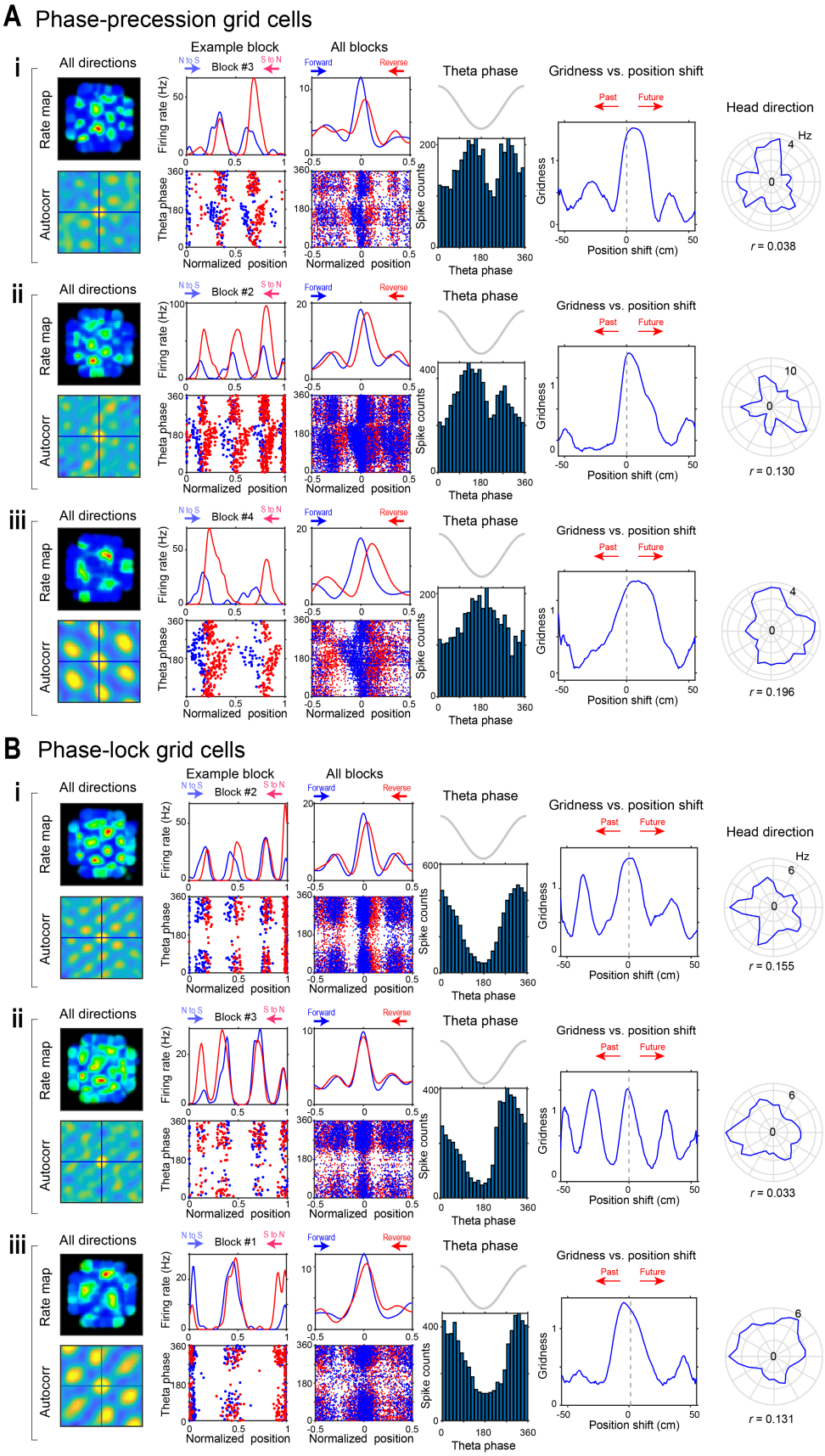
A Phase-precession grid cells
i
ii
iii
All directions
Rate map
Autocorr
Example block
All blocks
N to S
S to N
Forward
Reverse
Block #3
Block #2
Block #4
Firing rate (Hz)
Theta phase
Normalized position
Theta phase
Spike counts
Gridness vs. position shift
Past
Future
Gridness
Position shift (cm)
Head direction
Hz
r = 0.038
r = 0.130
r = 0.196
B Phase-lock grid cells
Block #2
Block #3
Block #1
r = 0.155
r = 0.033
r = 0.131

Fig. S4. Representative phase-precession and phase-locked grid cells.

(A) Three representative phase-precession grid cells (see also, Fig 2C). (Left) Firing rate maps (top) and their spatial autocorrelation (bottom) at the original positions. (Second and third left) Firing rate and spiking phases on theta oscillations in the linearized position in the example block and all blocks (Fig. S3 for the method). (Forth left) Theta phase preference of the cells. (Fifth left) Gridness scores as a function of reference positions. (Right) Firing rate modulation is by the head direction. The mean resultant length was indicated as *r*.

(B) Three representative phase-locked grid cells (see also, Fig 2D).

The firing properties of these cells (A & B) are highly consistent with previous reports (*13*).

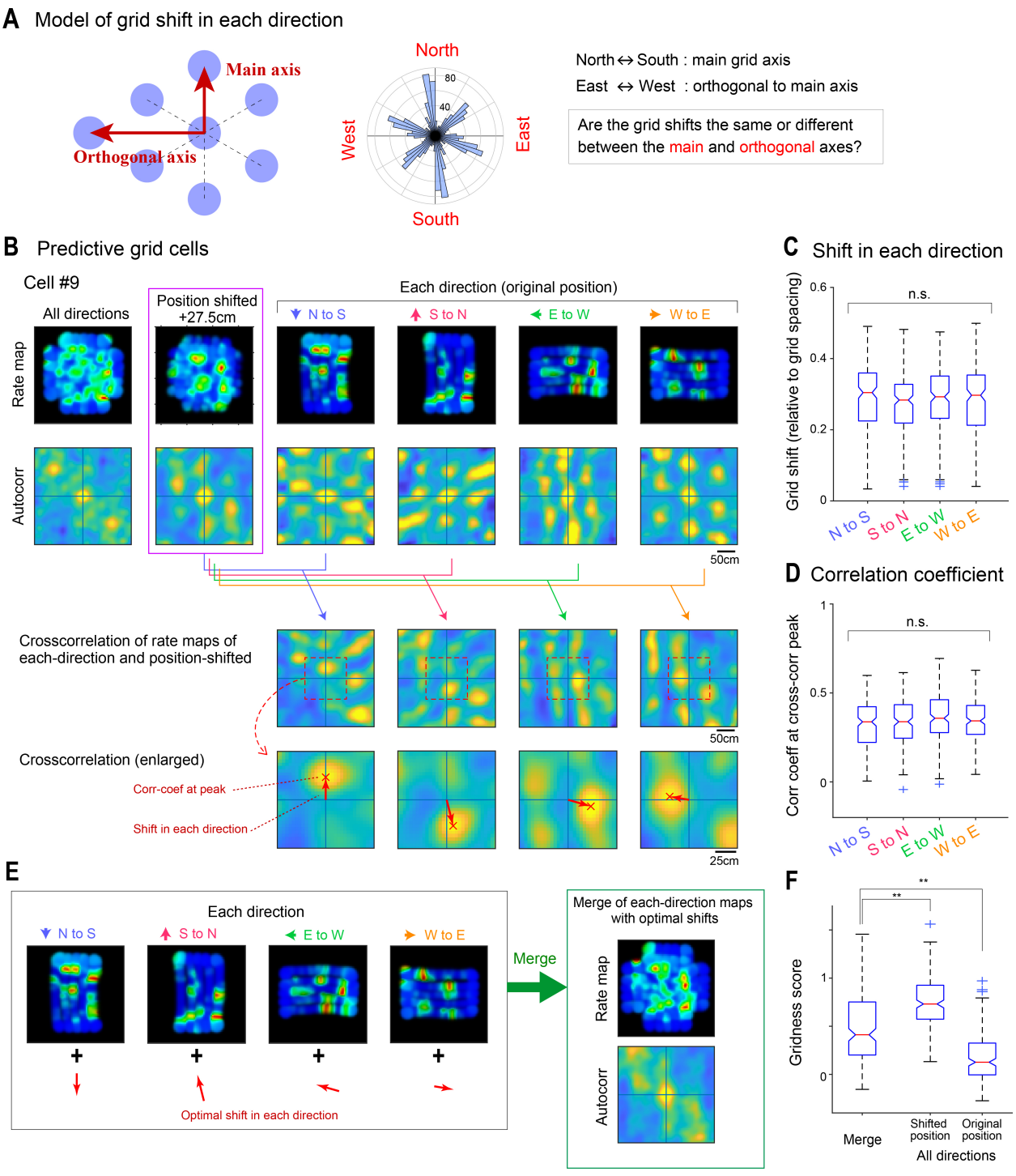

Fig. S5. Comparison of optimal grid shift in each direction in the predictive grid cells

(A) In the group analysis of the predictive grid cells, the optimal shift normalized by the grid spacing was 0.27 ± 0.11 (mean ± SD) (Fig 3G). On the other hand, when considering the hexagonal structure of the grid field, the grid spacing in the orthogonal axis is $\sqrt{3}$ times of that in the main axis. Here, we tested whether predictive grid cells have the same or different optimal shifts when running in the main and orthogonal axis directions. Since the north-south axis of the

open field was the main axis for all animals in this study (Fig 3L), we quantified the difference in the optimal shift between the north-south and east-west directions. (Left) Schematic of the main and orthogonal axes of the grid fields. (Right) Orientation of the grid axes of the predictive grid cells (same of Fig. 3L *left*).
(B) To estimate the optimal grid shift in each direction, we calculated cross-correlation of optimally shifted map of all direction and each unidirectional map, and quantified the offset of the cross-correlation peak from the center point. In the example shown here, the maps of cross-correlation of the optimally shifted map and each unidirectional map also showed the grid structure, with its maximum peak shifted against the direction of travel.
(C) Optimal grid shift in each direction, normalized by the grid spacing of the main axis. There were no significant differences of grid shift across running directions ($P>0.05$; ANOVA). The result showed that the optimal shift is tied to the grid spacing of the main axis, regardless the running direction.
(D) Correlation-coefficient at the peak of cross correlation map in each direction. There were no significant differences of grid shift across running directions ($P>0.05$; ANOVA).
(E) We verified whether merging the unidirectional maps with adding their optimal shifts reconstructs the optimally-shifted map in all directions.
(F) The merged map with the unidirectional maps with adding their optimal shifts had a significantly higher gridness score than the map at the original position. However, the gridness score of the merged map was significantly lower than that calculated for the optimally shifted map in all directions. $^{**}P<0.01$, ANOVA and post hoc Tukey-Kramer test.

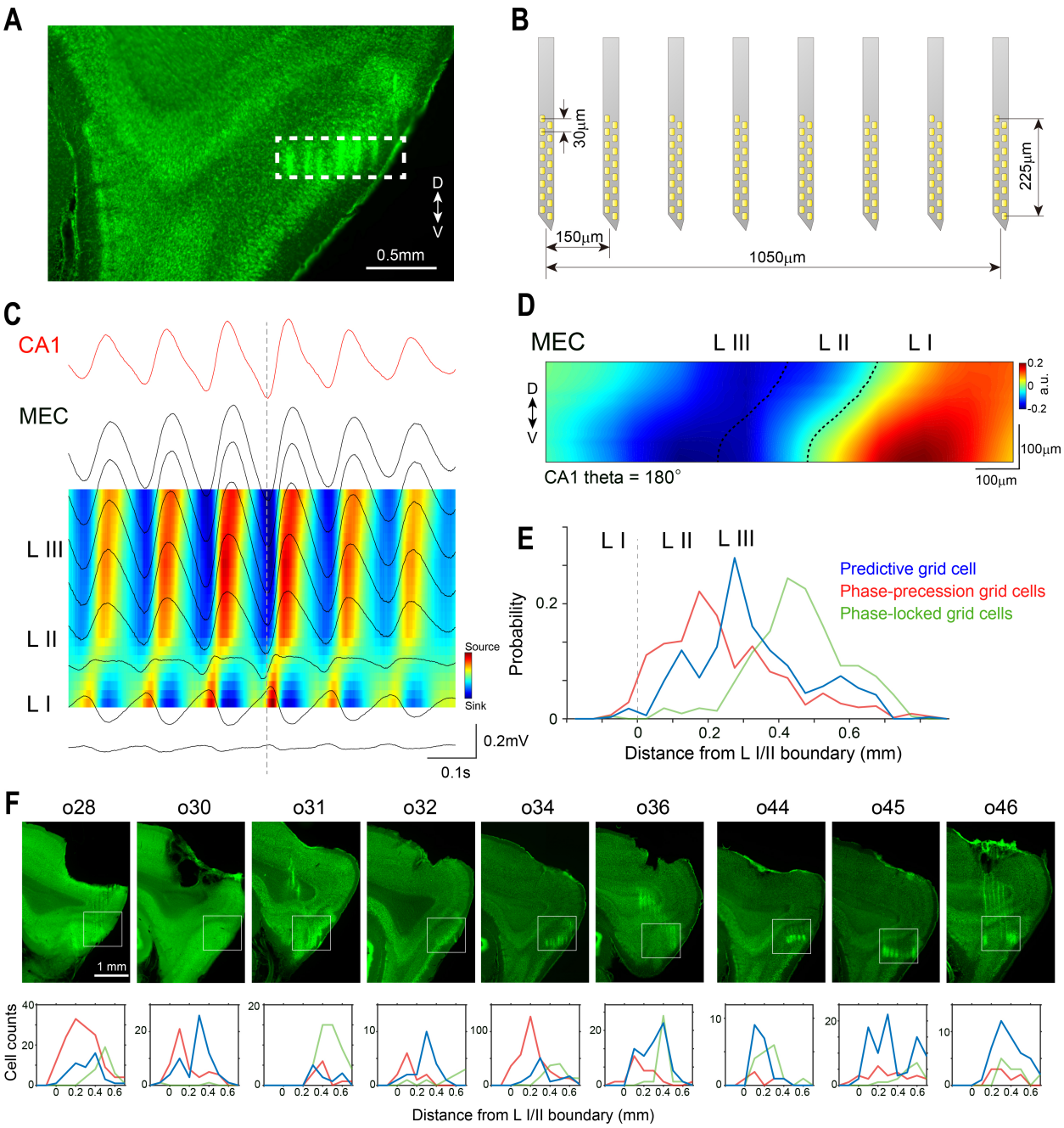

Fig. S6. Layer identification of the MEC neurons.

(A) Nissl-stained sections with electrode traces (indicated by a white dotted line) in the MEC (rat o34).

(B) Layout of shanks and electrodes of the 128-channel silicon probe. The eight shanks are spaced 150 μm apart, and 16 electrodes on each shank are staggered at intervals of 30 μm vertically and 16.5 μm horizontally.

(C) Plots of averaged LFPs (black lines) superimposed on a CSD color map in the MEC. LFPs were obtained from the center channels of all shanks. LFPs were filtered with the theta frequency band (4-10 Hz) and were aligned to the troughs of the CA1 theta.

(D) A two-dimensional CSD map of the MEC were constructed from all electrodes on the shanks. The averaged CSD at the trough timing (180°) of the CA1 theta is shown. Note that the anatomical boundaries between layers 1 and 2 correspond well with the reversal points of the CSD.
(E) Histograms of the recorded positions of predictive (blue), phase-precession (red), and phase-locked (green) grid cells. Predictive grid cells were mainly distributed in the relatively shallow positions of layer 3, and phase-locked grid cells were present in the relatively deep positions of layer 3. Phase-precession grid cells were mainly located in layer 2.
(F) Nissl-stained sections with electrode traces of all nine rats. (Bottom) Histograms of the recorded positions of predictive (blue), phase-precession (red), and phase-locked (green) grid cells in each rat.

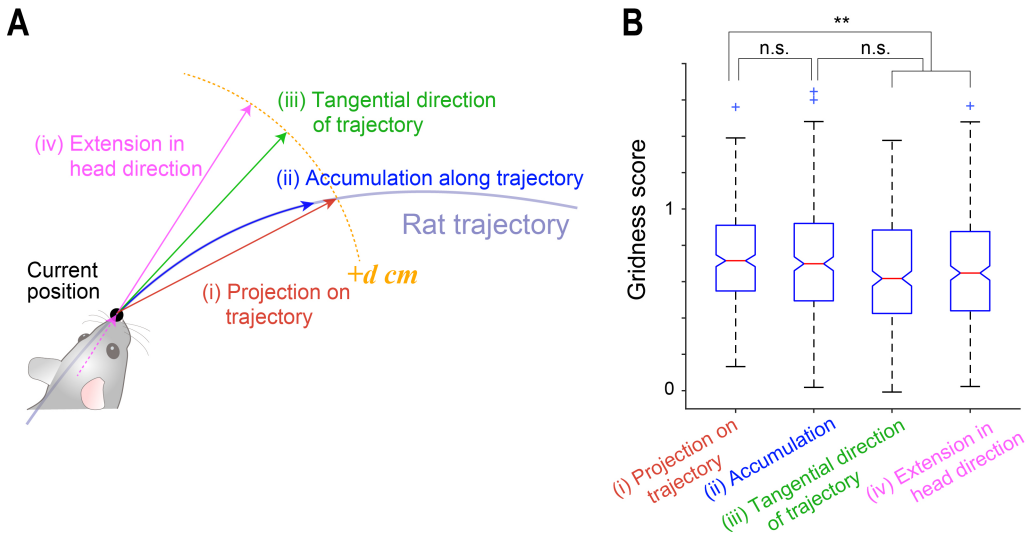

Fig. S7. Comparison of position projection methods.

(A) We tested the methods of spatial shift for estimating the gridness for the future position. (i) Projection on the rat trajectory with distance *d*, the method we used mainly in this study (Fig 1D). (ii) Accumulation along the trajectory. (iii) Projection on the tangential line of the rat trajectory. (iv) Projection on the line extended in the head direction.

(B) The gridness scores calculated with (i) and (ii) were not significantly different, whereas the gridness score with (i) were larger than those with (iii) or (iv). In this study, it was not possible to determine whether (i) or (ii) was greater due to the relatively low curvature of the rats' trajectories. $^{**}P<0.01$, ANOVA and post hoc Tukey-Kramer test.

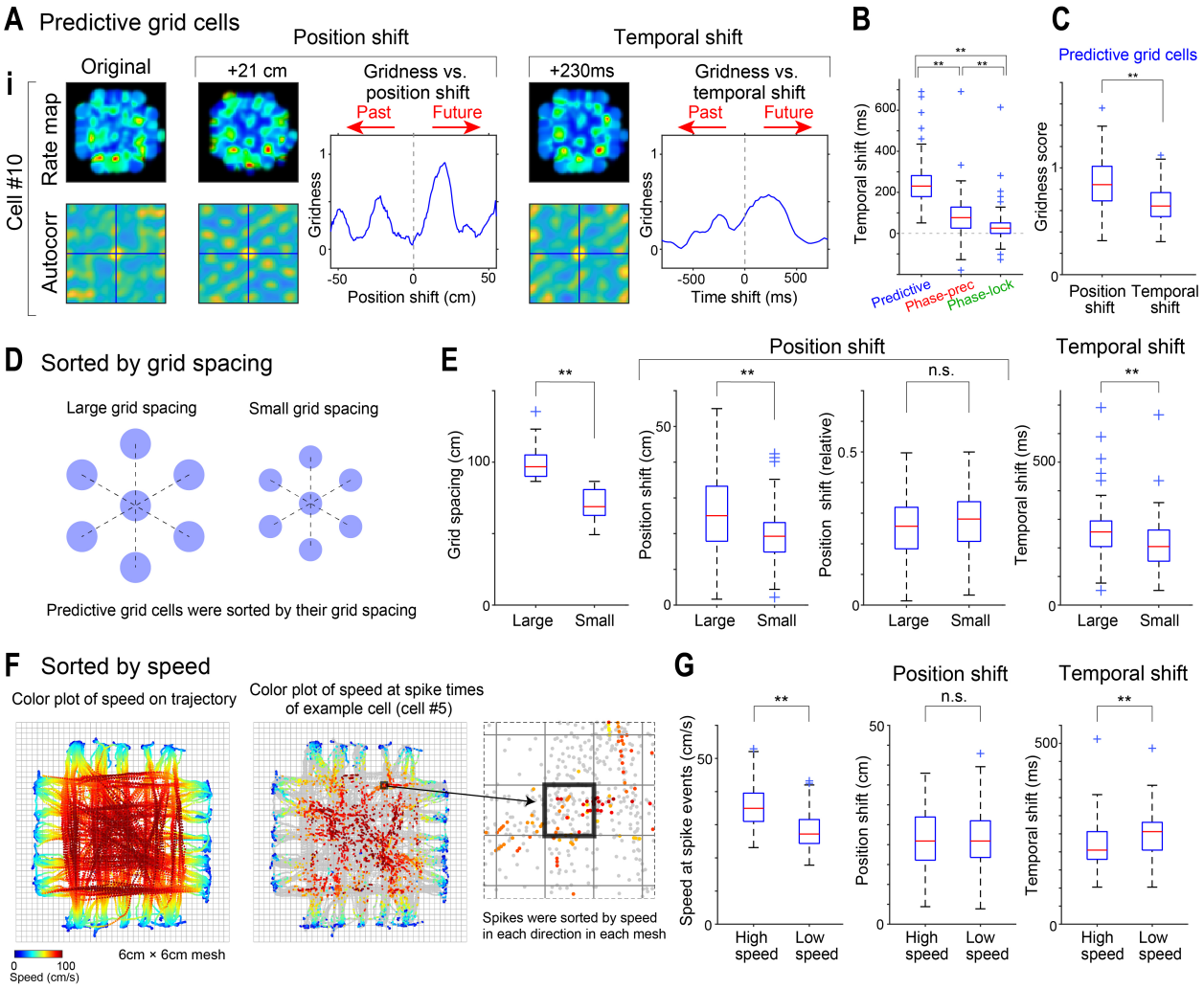

Fig. S8. Comparison of time and position shift for future projection.

(A) Firing patterns of a representative predictive grid cell, comparing time shift and position shift methods for future projection. (Left) Firing rate maps (top) and their spatial autocorrelations (bottom) at the original positions. (Middle) Firing rate maps, their spatial autocorrelation, and a plot of gridness as a function of position shift. (Right) Firing rate maps, their spatial autocorrelation, and a plot of gridness as a function of time shift.

(B) Optimal temporal shift in the predictive, phase-precession and phase-locked grid cells. $^{**}P<0.001$, ANOVA and post hoc Tukey-Kramer test.

(C) Gridness scores at optimal position and time shift of the predictive grid cells. The result showed that the position shift was higher than the time shift in the predictive grid cells. $^{**}P<0.01$, paired t-test.

(D) We further investigated the relationship between positional and temporal shifts in the predictive grid cells. To examine the effect of the size of the grid spacing on the spatial and temporal shift, we sorted the predictive grid cells by their grid spacing and divided them into two groups with large and small grid spacing. Then, the optimal position and time shifts were compared between the two groups. If the grid shift of the predictive grid cell is tied to the grid spacing, then the temporal shift should be larger in the cells with larger the grid spacing,

assuming constant speed. On the other hand, if the grid shift is tied to temporal variables, then the spatial shift normalized by grid spacing should be smaller in the cells with the larger the grid spacing.

(E) (Left) Grid spacing of the two groups of predictive grid cells sorted by their grid spacing. (Middle) Optimal position shift in cm (*middle left*) and normalized by grid spacing (*middle right*) of the predictive grid cells with larger and smaller grid cells. (Right) Optimal time shift of the predictive grid cells with larger and smaller grid cells. The result indicates that the grid shift of the predictive grid cells was tied to the grid spacing rather than the temporal variables. $^{**}P<0.01$, paired t-test.

(F) To examine the effect of running speed on spatial and temporal shift, spikes were sorted by speed in each predictive grid cell. If grid shift was tied to grid spacing, then the temporal shift should decrease at higher speed, assuming constant grid spacing. Conversely, if the grid shift is fixed to temporal variables, then the spatial shift normalized by grid spacing should increase at higher speeds. Regarding the sorting method, spike firings were sorted by speed in each predictive grid cell while preserving the positional information (SM). As shown here, there was an observed relationship between speed and rat position. To rule out the effect of position, we segmented the location into 6cm × 6cm meshes. Spikes were then sorted by speed in each mesh in each direction, dividing them into high and low-speed groups. Optimal position and time shifts were compared between these two speed groups. (Left) Speed at the rat's position in the example session. Each dot represents the position in a 25.6 ms bin, and its color indicates the speed. (Right) Speed at which the spike event occurred in the example cell. Each colored dot represents the position of the spike events, and its color indicates the speed. Gray dots indicate positions where the cell did not fire.

(G) (Left) Speed at the spike events, sorted by their speed, in each predictive grid cell. (Middle) Optimal position shift normalized by grid spacing in spikes with higher and lower speed of the predictive grid cells. (Right) Optimal time shift in spikes with higher and lower speed of the predictive grid cells. $^{**}P<0.01$, paired t-test. This result also showed that the grid shift of the predictive grid cells was tied to the grid spacing rather than the temporal variables. In the analysis in Fig. S8, we included the predictive grid cells that had a significant gridness score at the peak of both positional and temporal shifts (n = 168 cells).

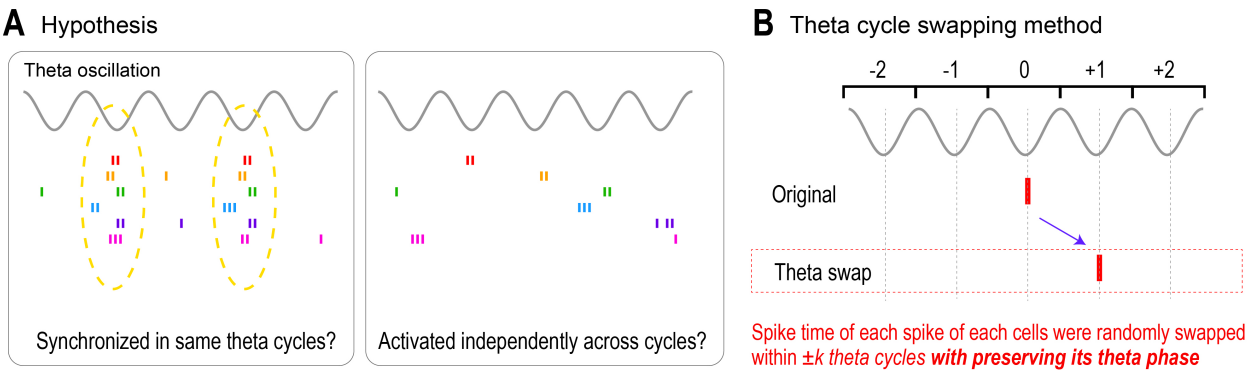
A Hypothesis
Theta oscillation
Synchronized in same theta cycles?
Activated independently across cycles?
B Theta cycle swapping method
-2
-1
0
+1
+2
Original
Theta swap
Spike time of each spike of each cells were randomly swapped within ±k theta cycles with preserving its theta phase

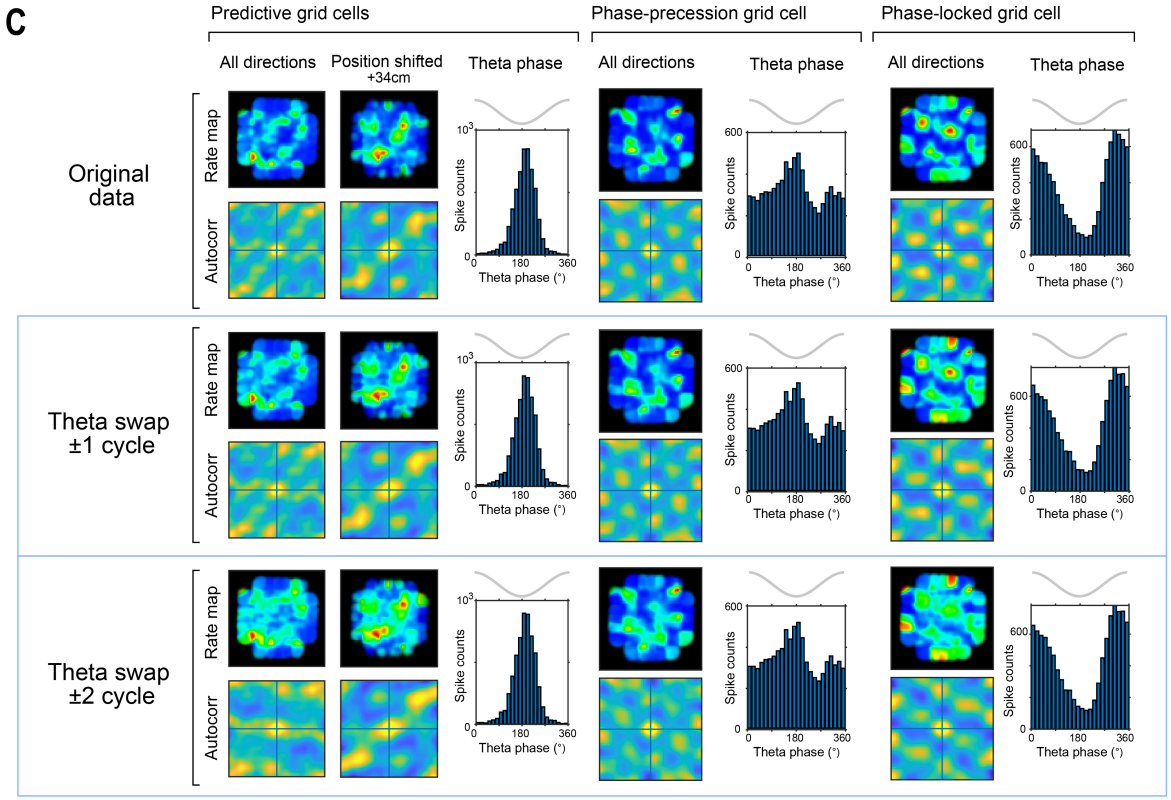
C
Predictive grid cells
Phase-precession grid cell
Phase-locked grid cell
All directions
Position shifted +34cm
Theta phase
Original data
Theta swap ±1 cycle
Theta swap ±2 cycle
Rate map
Autocorr
Spike counts
Theta phase (°)

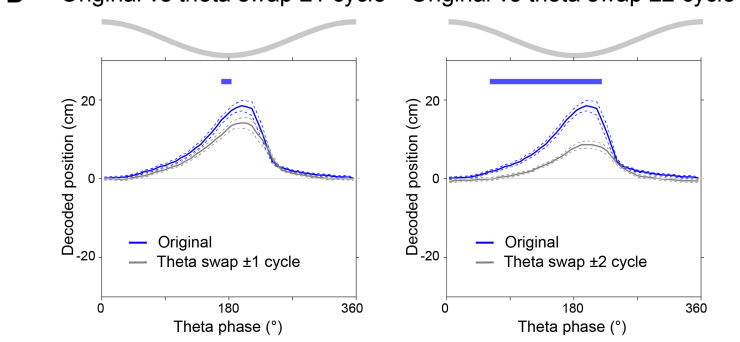
D
Original vs theta swap ±1 cycle
Original vs theta swap ±2 cycle
Decoded position (cm)
Original
Theta swap ±1 cycle
Theta swap ±2 cycle
Theta phase (°)

Fig. S9. Effect of synchronization on theta sequence formation.

(A) Hypotheses for the theta sequence analyzed in Fig 5. We examined whether the theta sequence was organized as a result of synchronized activity of cells within the theta cycle or as a result of independent activity of each cell.

(B) To address the above problem, we developed the theta-cycle swapping method. In this method, each spike of each cell is randomly swapped to a theta cycle with $\pm k$ cycle apart (k=1 or 2), preserving theta phase at the spike time. If the former model in (A) is correct, synchronization of spikes within the same theta cycles are important, so swapping theta cycle should result in reduction of decoding accuracy. On the other hand, if the latter model in (A) is correct, synchronization within a cycle is not important, so swapping spike times to a neighboring theta should not cause much change in decoding accuracy.

(C) The effect on the rate map of predictive, phase-precession and phase-locked grid cells when theta swap method is applied to cells (example cells). Theta cycle swapping had only a minor effect on the rate maps at least when $k = 1$.

(D) Decoded positional information (i.e., the argument of the maximum of probability densities) in the axis of the head direction as a function of theta phases (n = 25 sessions; SM; see also Fig. 5F). Blue lines indicate the decoding data with predictive, phase-precession, and phase-locked grid cells, and gray lines indicate those with theta swapping of spikes of these cells (mean ± SEM). A thick blue line above the plots indicates a segment with significantly higher values ($P <$ 0.01; permutation test; SM). Theta-swapped data had a significantly lower ability to decode the future positions around the 180° of theta oscillation than the original data. The result indicates that synchronized activity of cells within the theta cycle are critical for theta sequence formation.

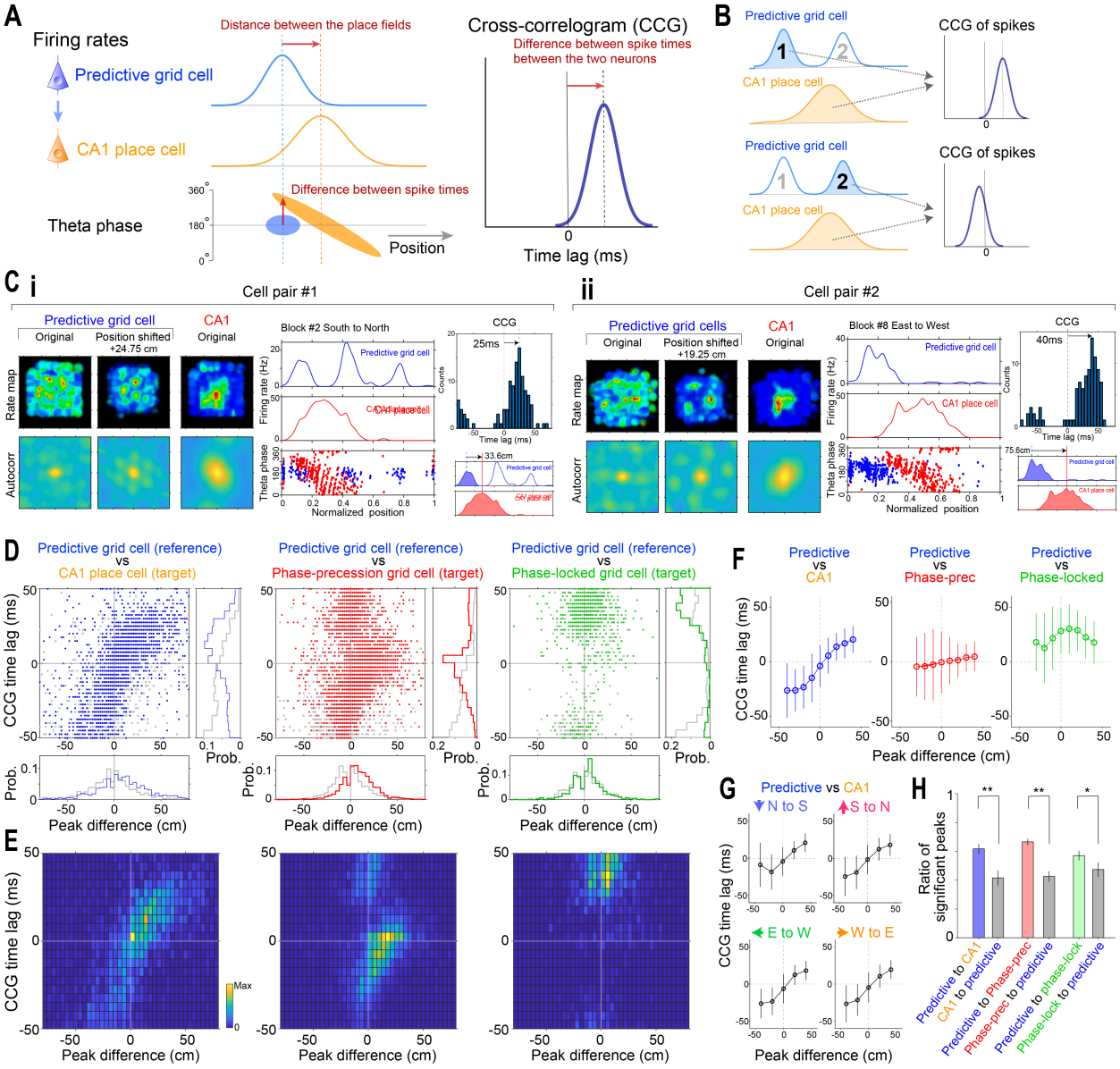

Fig. S10. Functional connectivity between predictive grid cells and CA1 place cells.

(A) Schematic of the relationship between spatial receptive fields and spike timing of predictive grid cells and CA1 place cells (see also Fig. 5G-H).

(B) If predictive grid cells and/or place cells had multiple peaks in the place fields (or grid fields), calculations were performed for each peak of each cell of the cell pair. All possible peak pairs were calculated, regardless of the preceding or following positional relationships. To estimate the peak difference, we used the one-dimensional rate plot calculated from the original positions. **(C)** The relationship between spike timings and place field distances of the pairs of predictive grid cells and CA1 place cells (**i-ii**, three representative pairs). (Left) Firing rate maps and autocorrelations of predictive grid cells and CA1 place cells. (Middle) Firing rate plots and spiking phases of predictive grid cells (blue) and CA1 place cells (red) in the linearized positions. (Right) CCGs of predictive grid cells and CA1 place cells from the selected positional

segments indicated in bottom insets. The values of CCG time lag and peak difference of firing rate peaks are also indicated.
(D) Group data of the relationships between spike timings and place field distances of the pairs of predictive grid cells and CA1 place cells (*left*), the pairs of predictive and phase-precession grid cells (*middle*), and the pairs of predictive and phase-locked grid cells (*right*). Each dot represents a CCG of a pair of single place fields of predictive grid cells and CA1 place cells (n = 3157 peak pairs from 1446 cell pairs of predictive grid cells and CA1 place cells), those of predictive and phase-precession grid cells (n = 6838 peak pairs from 2055 cell pairs of predictive and phase-precession grid cells), or those of predictive and phase-locked grid cells (n = 1297 peak pairs from 599 cell pairs of predictive and phase-locked grid cells). Colored and gray, significant and non-significant CCG peaks, respectively. (P<0.01, shuffling statistics; SM).
(E) Color plot of D. Only significant CCG peaks are selected.
(F) The relationship between the distance of place fields and time lag in CCG of the pairs of predictive grid cells and CA1 place cells (*left*), the pairs of predictive and phase-precession grid cells (*middle*), and the pairs of predictive and phase-locked grid cells (*right*).
(G) The relationship between the distance of place fields and time lag in CCG of the pairs of predictive grid cells and CA1 place cells, calculated for each running direction. The relations of the distance of place fields and time lags were not significantly different across the directions (P>0.05; two-way ANOVA).
(H) Ratio of the significant peaks of the CCGs of the pairs of predictive grid cells and CA1 place cells, the pairs of predictive and phase-precession grid cells, and the pairs of predictive and phase-locked grid cells (*right*). Colored bars indicate the pairs in which predictive grid cells fired before CA1 place cells (blue), phase-precession grid cells (red), or phase-locked grid cells (green) (i.e., CCG peak was at positive time lag), gray bars indicate the opposite case (i.e., CCG peak was at negative time lag). Clopper-Pearson confidence intervals (CIs) for 95% were shown ($^{*}P$<0.05, $^{**}P$<0.01).

Table S1. Basic physiology statistics.

Goal-direction task behavior

Rat ID	o28	o30	o31	o32	o34	o36	Total
Total sessions	13	15	6	7	21	8	70
Total RS neurons in MEC [1)]	524	1048	241	425	1356	249	3843
Predictive grid cells [2)]	48	61	11	20	113	52	305
Phase-precession grid cells [3)]	140	48	11	12	327	20	558
Phase-locked grid cells [4)]	38	2	48	8	122	23	241
Sessions for decoding [5)]	5	3			13	4	25
Figures that include the data	Figs 1, 2, 3, and 5; Figs S2-S10						

A series of goal-directed and random-foraging tasks

Rat ID	o44	o45	o46	Total
Total sessions	9	17	7	33
Total RS neurons in MEC [1)]	325	850	261	1436
Predictive grid cells [2)]	18	83	42	143
Phase-precession grid cells [3)]	5	30	9	44
Phase-locked grid cells [4)]	17	18	13	48
Figures that include the data	Fig. 4; Fig S6			

1) MEC regular spiking (RS) neurons were defined as those with mean firing rates between 0.8 and 7 Hz and with spatial information higher than 0.8 bit/spike (SM).
2) Predictive grid cells were defined as: (i) The gridness score at the original location is not significant ($P \geq 0.05$) compared to the shuffled data. (ii) When the gridness score is plotted as a function of location shift, there is a peak location at a future location, and the gridness score at the peak location is significant ($P < 0.05$). (iii) There is no phase precession, and theta phase preference is $180° \pm 60°$ with a peak-to-baseline ratio greater than 0.05 (SM).
3) Phase-precession grid cells were defined as (i) the gridness score at the original location is significant ($P < 0.05$) compared to the shuffled data, and (ii) phase precession is present (SM).
4) Phase-locked grid cells were defined as (i) the gridness score at the original location is significant ($P < 0.05$) compared to shuffled data, and (ii) there is no phase precession, and theta phase preference is $300° \pm 60°$ (SM).
5) Sessions in which more than 4 predictive grid cells and more than 4 grid cells were simultaneously recorded.

References and Notes

1. J. O'Keefe, L. Nadel, *The Hippocampus as a Cognitive Map* (Oxford Univ. Press, 1978).

2. T. E. J. Behrens, T. H. Muller, J. C. R. Whittington, S. Mark, A. B. Baram, K. L. Stachenfeld, Z. Kurth-Nelson, What is a cognitive map? Organizing knowledge for flexible behavior. *Neuron* **100**, 490–509 (2018).

3. B. L. McNaughton, F. P. Battaglia, O. Jensen, E. I. Moser, M. B. Moser, Path integration and the neural basis of the 'cognitive map'. *Nat. Rev. Neurosci.* **7**, 663–678 (2006).

4. G. Buzsáki, E. I. Moser, Memory, navigation and theta rhythm in the hippocampal-entorhinal system. *Nat. Neurosci.* **16**, 130–138 (2013).

5. T. Hafting, M. Fyhn, S. Molden, M. B. Moser, E. I. Moser, Microstructure of a spatial map in the entorhinal cortex. *Nature* **436**, 801–806 (2005).

6. F. Sargolini, M. Fyhn, T. Hafting, B. L. McNaughton, M. P. Witter, M.-B. Moser, E. I. Moser, Conjunctive representation of position, direction, and velocity in entorhinal cortex. *Science* **312**, 758–762 (2006).

7. T. Solstad, C. N. Boccara, E. Kropff, M. B. Moser, E. I. Moser, Representation of geometric borders in the entorhinal cortex. *Science* **322**, 1865–1868 (2008).

8. E. Kropff, J. E. Carmichael, M. B. Moser, E. I. Moser, Speed cells in the medial entorhinal cortex. *Nature* **523**, 419–424 (2015).

9. C. Wang, X. Chen, H. Lee, S. S. Deshmukh, D. Yoganarasimha, F. Savelli, J. J. Knierim, Egocentric coding of external items in the lateral entorhinal cortex. *Science* **362**, 945–949 (2018).

10. Ø. A. Høydal, E. R. Skytøen, S. O. Andersson, M. B. Moser, E. I. Moser, Object-vector coding in the medial entorhinal cortex. *Nature* **568**, 400–404 (2019).

11. R. J. Gardner, E. Hermansen, M. Pachitariu, Y. Burak, N. A. Baas, B. A. Dunn, M.-B. Moser, E. I. Moser, Toroidal topology of population activity in grid cells. *Nature* **602**, 123–128 (2022).

12. Y. Burak, I. R. Fiete, Accurate path integration in continuous attractor network models of grid cells. *PLOS Comput. Biol.* **5**, e1000291 (2009).

13. T. Hafting, M. Fyhn, T. Bonnevie, M. B. Moser, E. I. Moser, Hippocampus-independent phase precession in entorhinal grid cells. *Nature* **453**, 1248–1252 (2008).

14. J. Krupic, M. Bauza, S. Burton, C. Barry, J. O'Keefe, Grid cell symmetry is shaped by environmental geometry. *Nature* **518**, 232–235 (2015).

15. P. Chaudhuri-Vayalambrone, M. E. Rule, M. Bauza, M. Krstulovic, P. Kerekes, S. Burton, T. O'Leary, J. Krupic, Simultaneous representation of multiple time horizons by entorhinal grid cells and CA1 place cells. *Cell Rep.* **42**, 112716 (2023).

16. C. Barry, R. Hayman, N. Burgess, K. J. Jeffery, Experience-dependent rescaling of entorhinal grids. *Nat. Neurosci.* **10**, 682–684 (2007).

17. T. J. Davidson, F. Kloosterman, M. A. Wilson, Hippocampal replay of extended experience. *Neuron* **63**, 497–507 (2009).

18. T. Feng, D. Silva, D. J. Foster, Dissociation between the experience-dependent development of hippocampal theta sequences and single-trial phase precession. *J. Neurosci.* **35**, 4890–4902 (2015).

19. S. Terada, Y. Sakurai, H. Nakahara, S. Fujisawa, Temporal and rate coding for discrete event sequences in the hippocampus. *Neuron* **94**, 1248–1262.e4 (2017).

20. T. Danjo, T. Toyoizumi, S. Fujisawa, Spatial representations of self and other in the hippocampus. *Science* **359**, 213–218 (2018).

21. J. O'Keefe, M. L. Recce, Phase relationship between hippocampal place units and the EEG theta rhythm. *Hippocampus* **3**, 317–330 (1993).

22. W. E. Skaggs, B. L. McNaughton, M. A. Wilson, C. A. Barnes, Theta phase precession in hippocampal neuronal populations and the compression of temporal sequences. *Hippocampus* **6**, 149–172 (1996).

23. G. Dragoi, G. Buzsáki, Temporal encoding of place sequences by hippocampal cell assemblies. *Neuron* **50**, 145–157 (2006).

24. L. Acharya, Z. M. Aghajan, C. Vuong, J. J. Moore, M. R. Mehta, Causal influence of visual cues on hippocampal directional selectivity. *Cell* **164**, 197–207 (2016).

25. G. Ginosar, J. Aljadeff, Y. Burak, H. Sompolinsky, L. Las, N. Ulanovsky, Locally ordered representation of 3D space in the entorhinal cortex. *Nature* **596**, 404–409 (2021).

26. J. W. Rueckemann, M. Sosa, L. M. Giocomo, E. A. Buffalo, The grid code for ordered experience. *Nat. Rev. Neurosci.* **22**, 637–649 (2021).

27. L. M. Frank, E. N. Brown, M. Wilson, Trajectory encoding in the hippocampus and entorhinal cortex. *Neuron* **27**, 169–178 (2000).

28. K. L. Stachenfeld, M. M. Botvinick, S. J. Gershman, The hippocampus as a predictive map. *Nat. Neurosci.* **20**, 1643–1653 (2017).

29. F. P. Battaglia, G. R. Sutherland, B. L. McNaughton, Local sensory cues and place cell directionality: Additional evidence of prospective coding in the hippocampus. *J. Neurosci.* **24**, 4541–4550 (2004).

30. L. De Almeida, M. Idiart, A. Villavicencio, J. Lisman, Alternating predictive and short-term memory modes of entorhinal grid cells. *Hippocampus* **22**, 1647–1651 (2012).

31. R. U. Muller, J. L. Kubie, The firing of hippocampal place cells predicts the future position of freely moving rats. *J. Neurosci.* **9**, 4101–4110 (1989).

32. V. H. Brun, T. Solstad, K. B. Kjelstrup, M. Fyhn, M. P. Witter, E. I. Moser, M.-B. Moser, Progressive increase in grid scale from dorsal to ventral medial entorhinal cortex. *Hippocampus* **18**, 1200–1212 (2008).

33. K. Mizuseki, A. Sirota, E. Pastalkova, G. Buzsáki, Theta oscillations provide temporal windows for local circuit computation in the entorhinal-hippocampal loop. *Neuron* **64**, 267–280 (2009).

34. D. J. Foster, M. A. Wilson, Hippocampal theta sequences. *Hippocampus* **17**, 1093–1099 (2007).

35. D. Derdikman, J. R. Whitlock, A. Tsao, M. Fyhn, T. Hafting, M.-B. Moser, E. I. Moser, Fragmentation of grid cell maps in a multicompartment environment. *Nat. Neurosci.* **12**, 1325–1332 (2009).

36. J. Nagele, A. V. M. Herz, M. B. Stemmler, Untethered firing fields and intermittent silences: Why grid-cell discharge is so variable. *Hippocampus* **30**, 367–383 (2020).

37. M. Pröll, S. Häusler, A. V. M. Herz, Grid-cell activity on linear tracks indicates purely translational remapping of 2D firing patterns at movement turning points. *J. Neurosci.* **38**, 7004–7011 (2018).

38. J. R. Huxter, T. J. Senior, K. Allen, J. Csicsvari, Theta phase-specific codes for two-dimensional position, trajectory and heading in the hippocampus. *Nat. Neurosci.* **11**, 587–594 (2008).

39. A. M. Wikenheiser, A. D. Redish, Hippocampal theta sequences reflect current goals. *Nat. Neurosci.* **18**, 289–294 (2015).

40. K. Kay, J. E. Chung, M. Sosa, J. S. Schor, M. P. Karlsson, M. C. Larkin, D. F. Liu, L. M. Frank, Constant sub-second cycling between representations of possible futures in the hippocampus. *Cell* **180**, 552–567.e25 (2020).

41. S. E. Qasim, I. Fried, J. Jacobs, Phase precession in the human hippocampus and entorhinal cortex. *Cell* **184**, 3242–3255.e10 (2021).

42. J. O'Keefe, N. Burgess, Dual phase and rate coding in hippocampal place cells: Theoretical significance and relationship to entorhinal grid cells. *Hippocampus* **15**, 853–866 (2005).

43. N. Burgess, Grid cells and theta as oscillatory interference: Theory and predictions. *Hippocampus* **18**, 1157–1174 (2008).

44. A. Kamondi, L. Acsády, X. J. Wang, G. Buzsáki, Theta oscillations in somata and dendrites of hippocampal pyramidal cells in vivo: Activity-dependent phase-precession of action potentials. *Hippocampus* **8**, 244–261 (1998).

45. K. D. Harris, D. A. Henze, H. Hirase, X. Leinekugel, G. Dragoi, A. Czurkó, G. Buzsáki, Spike train dynamics predicts theta-related phase precession in hippocampal pyramidal cells. *Nature* **417**, 738–741 (2002).

46. M. R. Mehta, A. K. Lee, M. A. Wilson, Role of experience and oscillations in transforming a rate code into a temporal code. *Nature* **417**, 741–746 (2002).

47. Z. M. Aghajan, L. Acharya, J. J. Moore, J. D. Cushman, C. Vuong, M. R. Mehta, Impaired spatial selectivity and intact phase precession in two-dimensional virtual reality. *Nat. Neurosci.* **18**, 121–128 (2015).

48. S. J. Middleton, T. J. McHugh, Silencing CA3 disrupts temporal coding in the CA1 ensemble. *Nat. Neurosci.* **19**, 945–951 (2016).

49. M. I. Schlesiger, C. C. Cannova, B. L. Boublil, J. B. Hales, E. A. Mankin, M. P. Brandon, J. K. Leutgeb, C. Leibold, S. Leutgeb, The medial entorhinal cortex is necessary for temporal organization of hippocampal neuronal activity. *Nat. Neurosci.* **18**, 1123–1132 (2015).

50. C. Zheng, K. W. Bieri, Y. T. Hsiao, L. L. Colgin, Spatial sequence coding differs during slow and fast gamma rhythms in the hippocampus. *Neuron* **89**, 398–408 (2016).

51. N. T. M. Robinson, J. B. Priestley, J. W. Rueckemann, A. D. Garcia, V. A. Smeglin, F. A. Marino, H. Eichenbaum, Medial entorhinal cortex selectively supports temporal coding by hippocampal neurons. *Neuron* **94**, 677–688.e6 (2017).

52. A. Fernández-Ruiz, A. Oliva, G. A. Nagy, A. P. Maurer, A. Berényi, G. Buzsáki, Entorhinal-CA3 dual-input control of spike timing in the hippocampus by theta-gamma coupling. *Neuron* **93**, 1213–1226.e5 (2017).

53. C. Liu, R. Todorova, W. Tang, A. Oliva, A. Fernandez-Ruiz, Associative and predictive hippocampal codes support memory-guided behaviors. *Science* **382**, eadi8237 (2023).

54. L. M. Frank, E. N. Brown, M. A. Wilson, A comparison of the firing properties of putative excitatory and inhibitory neurons from CA1 and the entorhinal cortex. *J. Neurophysiol.* **86**, 2029–2040 (2001).

55. C. Barry, N. Burgess, Neural mechanisms of self-location. *Curr. Biol.* **24**, R330–R339 (2014).

56. M. Pachitariu, S. Sridhar, J. Pennington, C. Stringer, Spike sorting with Kilosort4. *Nat. Methods* **21**, 914–921 (2024).

57. A. Mathis, P. Mamidanna, K. M. Cury, T. Abe, V. N. Murthy, M. W. Mathis, M. Bethge, DeepLabCut: Markerless pose estimation of user-defined body parts with deep learning. *Nat. Neurosci.* **21**, 1281–1289 (2018).

58. P. Berens, CircStat: A *MATLAB* Toolbox for Circular Statistics. *J. Stat. Softw.* **31**, 1 (2009).

59. M. P. Brandon, A. R. Bogaard, C. P. Libby, M. A. Connerney, K. Gupta, M. E. Hasselmo, Reduction of theta rhythm dissociates grid cell spatial periodicity from directional tuning. *Science* **332**, 595–599 (2011).

60. R. F. Langston, J. A. Ainge, J. J. Couey, C. B. Canto, T. L. Bjerknes, M. P. Witter, E. I. Moser, M.-B. Moser, Development of the spatial representation system in the rat. *Science* **328**, 1576–1580 (2010).

61. K. Mizuseki, K. Diba, E. Pastalkova, G. Buzsáki, Hippocampal CA1 pyramidal cells form functionally distinct sublayers. *Nat. Neurosci.* **14**, 1174–1181 (2011).

62. W. E. Skaggs, B. L. McNaughton, K. M. Gothard, E. J. Markus, "An information-theoretic approach to deciphering the hippocampal code" in Advances in Neural Information Processing Systems, vol. 5, S. J. Hanson, J. D. Cowan, C. J. Giles, Eds. (Morgan Kaufmann, 1993), pp. 1030–1037.

63. J. J. Chrobak, G. Buzsáki, Gamma oscillations in the entorhinal cortex of the freely behaving rat. *J. Neurosci.* **18**, 388–398 (1998).

64. A. Fernández-Ruiz, A. Oliva, M. Soula, F. Rocha-Almeida, G. A. Nagy, G. Martin-Vazquez, G. Buzsáki, Gamma rhythm communication between entorhinal cortex and dentate gyrus neuronal assemblies. *Science* **372**, eabf3119 (2021).

65. K. Zhang, I. Ginzburg, B. L. McNaughton, T. J. Sejnowski, Interpreting neuronal population activity by reconstruction: Unified framework with application to hippocampal place cells. *J. Neurophysiol.* **79**, 1017–1044 (1998).

66. S. Fujisawa, A. Amarasingham, M. T. Harrison, G. Buzsáki, Behavior-dependent short-term assembly dynamics in the medial prefrontal cortex. *Nat. Neurosci.* **11**, 823–833 (2008).